Picrasma quassioides mediated cerium oxide nanostructures and their post-annealing treatment on the microstructural, morphological and enhanced catalytic performance

T.V.M. Sreekanth[a], G.R. Dillip[b], Yong Rok Lee[a],*

[a]*Department of Chemical Engineering, Yeungnam University, Gyeongsan 712-749, Republic of Korea*
[b]*School of Mechanical Engineering and Technology, Yeungnam University, Gyeongsan 712-749, Republic of Korea*

Abstract

Cerium oxide (CeO_2) nanostructures are an interesting metal oxide in catalysis owing to their unique redox properties and high mobility of oxygen vacancies at the surface. CeO_2 nanostructure was synthesized via a green route using an aqueous extract of *Picrasma quassioides* bark. Formation of ceria nanostructures were monitored by UV–vis absorption spectroscopy and Fourier transform infrared spectroscopy (FTIR). Annealing temperature-dependent crystallite size and lattice strain on the X-ray peak broadening of the CeO_2 nanostructures was determined by the size–strain plots. The application of the green synthesized CeO_2 nanostructures for the catalytic degradation of methylene blue by $NaBH_4$ was carried out. We demonstrated that the catalytic decomposition rate was gradually improved due to the increase of annealing temperature of CeO_2 nanostructure, and obtained highest performance at 600 °C annealed sample. This is because of the significantly improved crystallinity of CeO_2 nanostructure at higher temperature, leading in a low density of crystalline defects and wide distribution of nanostructure with a large surface area to provide more active electrons (e^-) for the decomposition of dye.
© 2016 Elsevier Ltd and Techna Group S.r.l. All rights reserved.

1. Introduction

Cerium (Ce) is one of the most abundant rare earth elements in the earth's crust, comprising approximately 66 ppm in free metal or oxide form [1]. Cerium oxide (CeO_2) is a semiconductor with a wide band gap (3.19 eV) and large exciton binding energy [2]. In recent years, CeO_2 nanomaterials have attracted attention because of their unique physical and chemical properties that are significantly different from those of bulk materials [3]. Therefore, they have been used in a wide range of applications, such as catalyst [4], gas sensors [5], polishing materials [6], solid oxide fuel cells [7], sunscreen lotions [8], ultraviolet absorbers [9], electronics [10], agriculture [11], optical devices [12], drug delivery [13], and in the field of biomedical applications.

In general, CeO_2 nanomaterials have been synthesized using physical and chemical methods, including hydrothermal [14], microwave [15], sonochemical [16], sol–gel [17], solvothermal [18], flame spray pyrolysis [19], ball milling [20], thermal decomposition [21], and co-precipitation [22]. On the other hand, these methods are complex, required long time physical and chemical reactions, the use of toxic chemicals, high pressures and temperatures, and potentially hazardous to the environment. Green synthesis methods are inexpensive, safe and easy to use, do not produce any toxic byproducts, and are an eco-friendly alternative to physical or chemical methods. On the other hand, there are only a few reports available on the green synthesis of CeO_2 nanomaterials in the literature using a range of biomaterials, such as honey [23], *Gloriosa superba* L. leaf [24] and *Aloe barbadensis* miller gel [25].

*Corresponding author. Tel.: +82 53 810 2529; fax: +82 53 810 4631.
E-mail address: yrlee@yu.ac.kr (Y.R. Lee).

Picrasma quassioides (*P. quassioides*) (D. Don) Bennett (family Simaroubaceae) is a species of *Picrasma* native to the temperate regions of southern Asia. The plant branches are used as a traditional folk medicine for the treatment of a variety of diseases, such as hypertension, cancer, snake bites, and gastroenteritis [26,27]. In the present investigation, CeO_2 nanostructure was synthesized by using *P. quassioides* bark aqueous extract. To the best of our knowledge, there are no reports of the synthesis of CeO_2 nanostructures using an aqueous extract of *P. quassioides* bark. The aim of the present study is to explore the effect of post-annealing treatment of the synthesized nanostructures to improve their crystallinity. The application of annealing temperature-dependent of CeO_2 nanostructures for the enhanced catalytic decomposition of methylene blue (MB) by $NaBH_4$ was carried out.

2. Experimental

2.1. Chemicals

A high purity (99.9%) analytical reagent grade (AR) cerium chloride heptahydrate ($CeCl_3.7H_2O$), sodium borohydride ($NaBH_4$) and methylene blue ($C_{16}H_{18}ClN_3S.3H_2O$) were purchased from Sigma-Aldrich (Seoul, South Korea). The chemicals were used as purchased without further purification. The *P. quassioides* bark was purchased from a local oriental market in Gyeongsan, South Korea.

2.2. Synthesis of CeO_2 nanostructures

First, the *P. quassioides* bark was ground to a fine powder. Subsequently, 5 g of dry *P. quassioides* bark powder was mixed with 100 mL of deionized water in a beaker, stirred at 60 °C for 30 min and thereafter, filtered through Whatman no: 42 filter paper. The required quantity of cerium chloride heptahydrate (3.72 g) was dissolved in 100 mL of the *P. quassioides* bark extract. The resulting solution was stirred at 80 °C for 6 h and allowed to cool naturally to room temperature (RT). A yellowish brown precipitate was formed, and the supernatant was discarded. The obtained precipitation was dried in a vacuum oven at 80 °C for 4 h to get CeO_2 nanostructure. Finally, the as-prepared powders were calcined at three various temperatures at 200, 400 and 600 °C for 2 h in air to further study their structural, morphological and catalytic activity of CeO_2 nanostructures. The sintered products were denoted as CeO_2-200, CeO_2-400 and CeO_2-600 for 200, 400 and 600 °C annealed temperatures, respectively.

2.3. Characterization

The green synthesized CeO_2 nanostructures were monitored using a double beam UV–vis spectrophotometer (OPTIZEN-3220UV) over the wavelength range of 200–800 nm. Dried samples of the *P. quassioides* bark extract and CeO_2 nanostructure was pelletized separately with KBr and examined by Fourier transform infrared spectroscopy (FT-IR, Perkin-Elmer-Spectrum Two). The morphology of the green synthesized

CeO_2 nanostructures were examined by using high-resolution transmission electron microscopy (HR-TEM, Tecnai G2 F20 S-Twin, USA) operating at an accelerating voltage of 200 kV with a point resolution of 0.24 nm and a Cs of 1.2 mm. To prepare a sample of TEM, a small amount of powder was first dispersed in water, sonicated for 5 min and thereafter drop-coated on a commercially available carbon-coated copper grid. This was dried under a visible-light for 10 min. The length scales are indicated systematically as a black bar on the bottom corner of the images. Atomic force microscopy (Tapping mode-Nanoscope III a, Digital Instruments, Inc.) was used for topographic analysis of the CeO_2 nanostructures. The polycrystalline nature of green synthesized CeO_2 nanostructures were examined by X-ray diffraction (XRD, PANalytical X'Pert³ PRO, USA) using Cu Kα radiation ($\lambda = 1.54$ Å) at 40 kV and 30 mA. The chemical state and composition of the elements present in the CeO_2 nanostructure was identified by X-ray photoelectron spectroscopy (XPS, Thermo Scientific K-Alpha) using a Al Kα X-ray source (1486.6 eV). The source energies of 200 eV and 30 eV were used for the high and low-resolution scans, respectively.

2.4. Catalytic activity of CeO_2 nanostructures

To ascertain catalytic activity of CeO_2 nanostructures, the degradation of the synthetic organic dye, Methylene blue (MB) by $NaBH_4$ using CeO_2 nanostructure as a catalyst was carried out [28]. MB is used widely as a redox indicator in analytical chemistry. The aqueous solution of this substance is blue in an oxidizing environment, and turns to colorless when exposed to reducing agents. Its redox properties can be observed in a classical demonstration of chemical kinetics in an experiment known as the "*blue bottle*" experiment. Moreover, MB can be used as a staining dye in many reactions as Wright's stain and Jenner's. In a typical experiment, 5 ml of $NaBH_4$ (0.01 M) mixed with 50 ml of an aqueous solution of MB (1×10^{-3} M) in a beaker, and 30 mg of CeO_2 nanostructure was then rapidly added to the above mixture with constant stirring. The color of the mixture vanished gradually, indicating the reduction of MB. The catalytic activity of the CeO_2 nanostructure was evaluated by monitoring the variation in absorbance intensity of the dye solution as a function of time at the corresponding wavelength using an UV–vis spectrophotometer (OPTIZEN-3220UV). To understand the effect of size/impurity on the catalytic activity of the CeO_2 nanostructure, the catalytic experiments were conducted using various annealed samples (CeO_2-200, CeO_2-400 and CeO_2-600) as an active catalyst for the degradation of MB by $NaBH_4$.

3. Results and discussion

The *P. quassioides* bark aqueous extract was used as a capping and reducing agent for the synthesis CeO_2 nanostructures. A typical UV–vis absorbance spectrum of CeO_2 nanostructure is shown in Fig. 1. In general, cerium in the 3^+ state (III) could absorb the energy in both ultraviolet (UV) and visible regions, whereas the 4^+ state (IV) absorbs only in the
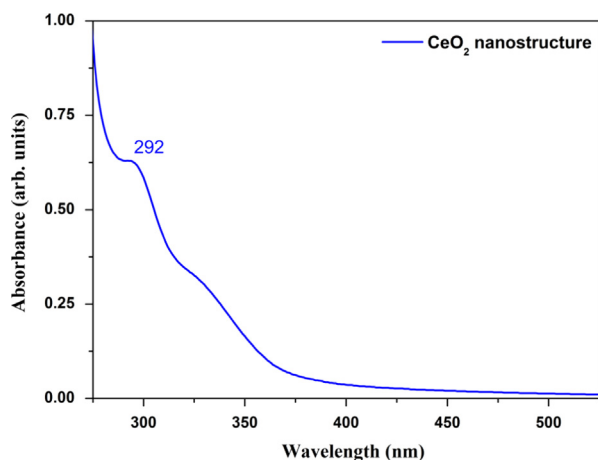
Fig. 1. UV–visible absorption spectrum of the green synthesized CeO$_2$ nanostructure.
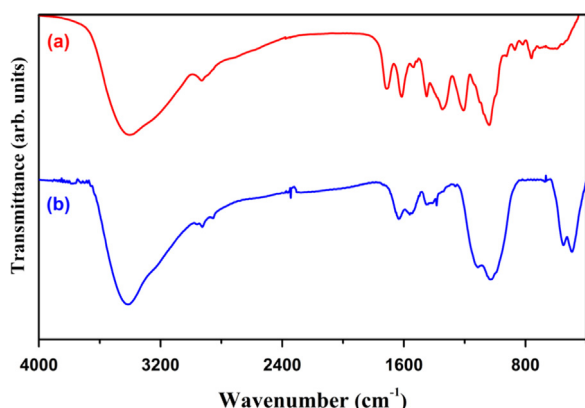

Fig. 2. FT-IR spectra of (a) *P. quassioides* extract and (b) CeO$_2$ nanostructure.

visible region. As expected, a characteristic absorption peak at 298 nm was confirmed the formation of CeO$_2$ nanostructure that crystalized in a simple cubic structure [29,30]

Typical FT-IR spectra of the green synthesized CeO$_2$ nanostructure and the bark extract are shown in Fig. 2. The FT-IR spectrum of *P. quassioides* bark consist of several absorption bands at 3404 cm^{-1} (O–H stretch; alcohols and phenols), 2929 cm^{-1} (O–H stretch; alkanes); 1713 cm^{-1} (C=O stretch; carboxylic acids), 1613 cm^{-1} (N–H bend 1° amines), 1449 cm^{-1} (C–H stretch (in-ring), aromatics), 1346 cm^{-1} (N–O symmetric stretch, nitro compounds), 1207 cm^{-1} (C–O stretch, alcohols, carboxylic acids, esters and ethers), 1039 cm^{-1} (C–N stretch, aliphatic amines), and 870 and 760 cm^{-1} (bend alkenes). In the FT-IR spectrum of the CeO$_2$ nanostructure, the bands were located at about 3410 cm^{-1}, correspond to the –OH stretching from residual alcohols, water and Ce–OH [24]. The band at 1031 cm^{-1} is due to the (Ce–O–Ce) vibration [31]. The peak near 1641 cm^{-1} was assigned to the bending vibration of H–O–H that partially overlapped with the O–C–O stretching band. The bands between 700 and 400 cm^{-1} were assigned to the Ce–O stretching vibration [32]. Based on these results, *P. quassioides* bark contains alcohols, phenols, carboxylic acids, 1° amines,

aromatics, alkanes, and alkenes. These biomolecules are responsible for the formation and stabilization of the synthesized CeO$_2$ nanostructures.

Fig. 3(a) presents a comparison of the XRD pattern of green synthesized CeO$_2$ nanostructures (CeO$_2$-200, CeO$_2$-400 and CeO$_2$-600) and standard CeO$_2$ crystallographic data. All the reflections obtained for the CeO$_2$ nanostructures were well matched to the standard crystallographic data, Joint Committee on Powder Diffraction Standards (JCPDS): 034-0394. For all samples, the peaks at about 28.55, 33.08, 47.47, 56.33, 59.08, 69.40, 76.70, 79.07 and 88.41° were assigned to the (111), (200), (220), (311), (222), (400), (331), (420) and (422) planes, respectively. The standard XRD peaks confirmed the common cubic structure (JCPDS no: 034-0394) of the synthesized CeO$_2$ nanostructure. No other impurity phases are identified, which are indicating the high purity of the annealed samples. However, a closer look certainly indicates that the peak position of the all XRD peaks was shifted toward higher angle side as a function of annealing temperature. The dominant XRD peak shifting is shown in Fig. 3(b). We note from the figure that the crystallinity of the samples increased as the increase of annealing temperature. And also full-width at half-maxima (FWHM) values of the nanostructures was decreased with the temperature. The XRD patterns were refined using celref3 software provided by collaborative computational project number 14 (CCP14). The method used to refine the lattice parameter was a least squares refinement [33], and the refined values are listed in Table 1. As noted from the table, the volume of the nanostructures are found to be decreased (lattice contraction) with the raise of temperature. To corroborate the lattice contraction of nanostructures, the temperature dependent size–strain values were estimated using the X-ray peak broadening method. The formulae and method used to calculate the size–strain are reported in our previously published papers [34,35]. The plots of $\frac{1}{\beta_D}$ (x-axis) and $\cos\theta$ (y-axis) are shown in Fig. 3(c). All the samples were fitted to the linear function and the crystallite size D is calculated from the slope of the fits. The values of D for all annealed samples are listed in Table 1. As seen in the table, the crystallite size values are increased due to the increase of annealing temperature. This is because of narrowing of the XRD peaks with the temperature (Fig. 3(b)). The size–strain plots are plotted for all samples that resulted in straight lines as shown in Fig. 3(d). As shown in the figure, all samples were fitted to the linear equation and further estimated the strain and size values from the slope and y-intercept of the curves, respectively. The calculated values are tabulated in Table 1. The crystallite size values are well consistent with the values calculated from the $\frac{1}{\beta_D}$ and $\cos\theta$ plots (Fig. 3(c)). We note from the table that the strain values are increased as a function of annealing temperature. A negative strain is due to the relaxed crystallites; on the other hand the positive value of micro-strain is because of the contraction of crystallites [36]. Therefore, the −ve sign indicates that lattice contraction was observed due to the increase of annealing temperature, corroborated by the volume values of nanostructures (Table 1). In general, the strain would be releases in bigger particles. In the current case, due to the
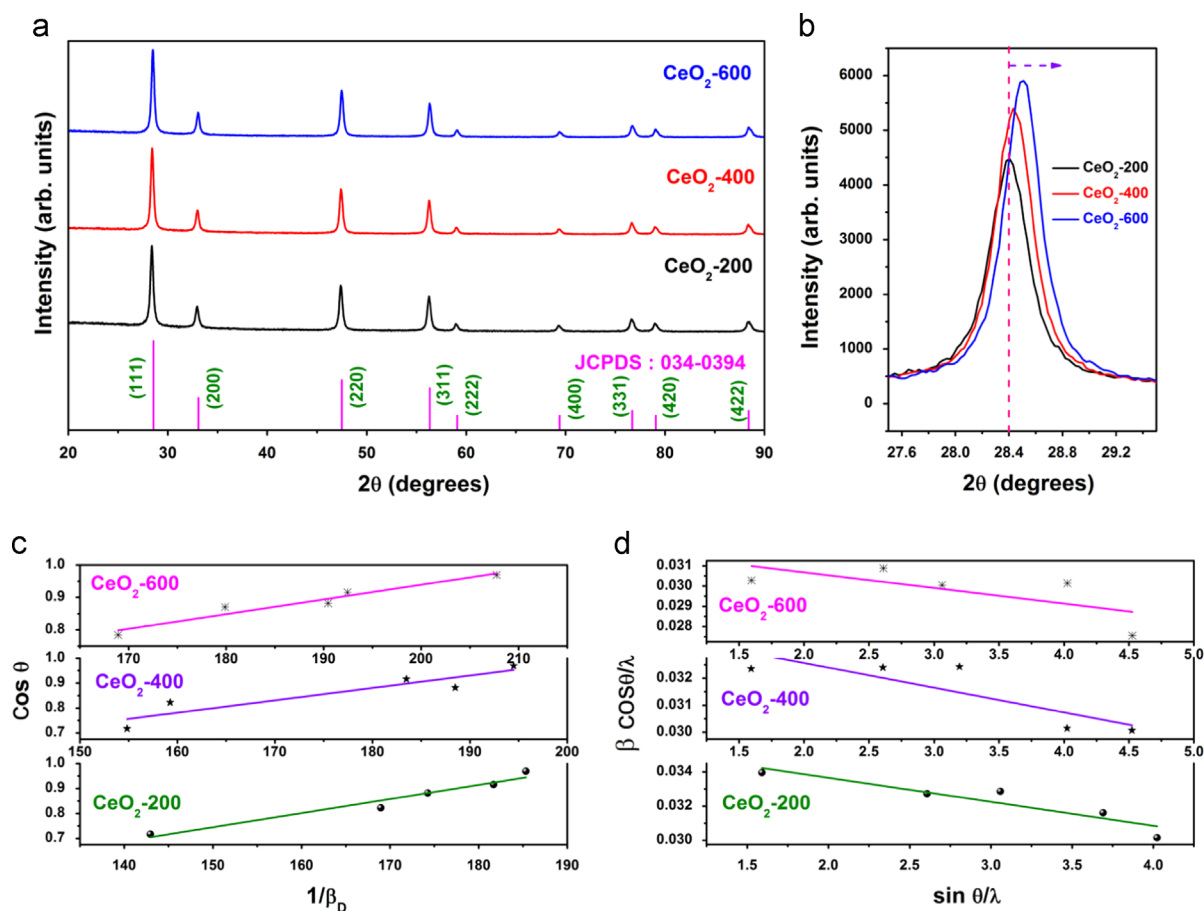
Fig. 3. (a) XRD patterns and (b) their corresponding magnified view of dominant XRD peak, (c) plot of cos θ versus $1/\beta_D$, and (d) size–strain plot of the annealed CeO$_2$ nanostructures.

Table 1
Lattice parameter (a), volume (V), crystallite size and strain values of CeO$_2$ nanostructures.

Sample	a (nm)	Volume (nm^3)	Scherrer method D (nm)	Size–strain plot method	
				D (nm)	ε ($\times 10^{-4}$)
CeO$_2$-200	0.543933	0.160930	24.53	24.68	-3.50
CeO$_2$-400	0.543292	0.160362	27.95	26.16	-2.28
CeO$_2$-600	0.541855	0.159092	30.60	27.93	-1.92

increase of annealing temperature, the crystallite sizes are increased that resulted in increase of strain values. Therefore, the effect of annealing temperature causes size–strain effects in the nanostructures that affect the catalytic properties of the nanostructures greatly.

TEM images of the annealed CeO$_2$ nanostructures are shown in Fig. 4. As shown in the figure, the annealed samples were well dispersed, similar to appear and however, possess various morphologies. Some of them are appear to be spherical, triangular, tetragonal, octahedral, etc [37]. Although the nanostructures are similar to appear for all samples, as expected, the aggregation of particles were decreased as the increase of annealing temperature. The particle/grain size variations have not observed clearly in the TEM images because of the wide distribution of nanostructures, however; the grain sizes were approximately found to be in the range of 10–80 nm. To confirm the phase formation of CeO$_2$ nanostructures, the HR-TEM images were analyzed using Gatan software. The HR-TEM images of CeO$_2$-200, 400 and 600 nanostructures are shown in Fig. 4(d), (g) and (j) and insets of corresponding figures show their magnified versions (f, i and l) and line profiles (e, h and k) of HRTEM, respectively. The lattice fringe distance of 0.306 nm (CeO$_2$-200), 0.305 nm (CeO$_2$-400) and 0.303 nm (CeO$_2$-600) were assigned to the (111) plane of the CeO$_2$ structure. These values are good agreement with the XRD data. Therefore, the HRTEM images revealed the good crystalline nature of the annealed samples.

The surface roughness calculation using atomic force microscopy measurements is an indirect way but very effective way to qualitatively determine the active surface sites on the thin film surface. Therefore, the AFM images of the annealed samples were recorded. The surface roughness of all annealed samples (not shown here) was estimated and those values are increased with an increase of annealing temperature as the following: CeO$_2$-200 < CeO$_2$-400 < CeO$_2$-600. The highest surface roughness for CeO$_2$-600 (with respective to other samples) is because of the higher crystallinity and lower aggregation of sample at 600 °C temperature.
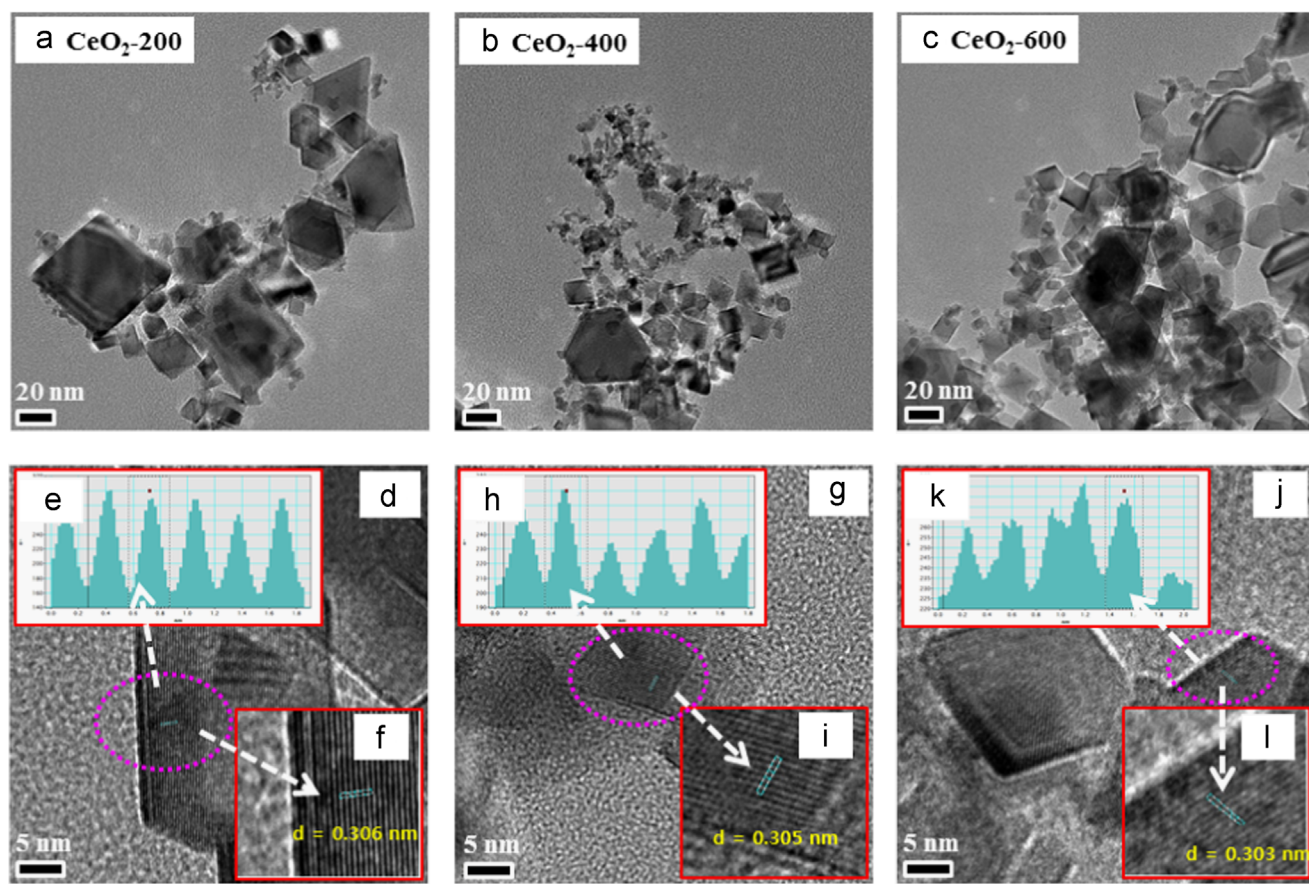
Fig. 4. (a)–(c) Low magnification, (d, g and j) high magnification HR-TEM images and their corresponding magnified view of HR-TEM images (f, i and l) showing d-spacing values and line profiles (e, h and k) of CeO₂-200, 400 and 600 nanostructures, respectively.

To identify surface properties of the annealed CeO_2 nanostructure, the XPS analysis was performed. XPS provides information on the oxidation state of each element in the sample. Fig. 5(a) shows the survey spectrum of CeO_2-400 nanostructure. The spectrum revealed the presence of C, O and Ce without other impurities, confirming the phase purity of the synthesized nanostructure. The presence of carbon in the sample was attributed to carbon contained in the bark extract used for the reduction of the CeO_2. To find more detailed information regarding the state of the elements, the high-resolution spectra of C 1s, O 1s and Ce 3d were recorded and shown in Fig. 5(b–d). The C 1s core level spectrum composed of three sub-components (C1, C2 and C3). The peaks at 285.6 eV (C1), 289.7 eV (C2) and 293.6 eV (C3) are assigned to the hydrocarbon phase, plasmon transition and carbonate species, respectively. Fig. 5(c) represents the Gaussian fitted core level spectrum of O 1s. The decomposed spectrum consisted of four peaks at binding energies of 529.8 eV (O1), 530.8 eV (O2), 531.9 eV (O3), and 534.1 eV (O4). The peak at O1 (529.8 eV) from the lattice oxygen was attributed to O_2^- ions surrounded by Ce^{4+} ions, which corresponds to the Ce–O bond in the CeO_2 nanostructure. The binding energy at O2 (530.8 eV) can be assigned to O_2^- ions in the Ce–O bond, where cerium is present in the Ce^{3+} state. The peak at O3 (531.9 eV) correspond to oxygen

vacancies. The peak at a higher binding energy O4 (534.1 eV) was not associated with the presence of either of Ce^{4+} or Ce^{3+} and was assigned to adsorbed water or –OH on the surface of the CeO_2 nanostructure. The Ce 3d narrow scan was deconvoluted into several components (Fig. 5(d)), which are located at 883.1 eV (Ce1), 884.9 eV (Ce2), 886.5 eV (Ce3), and 889.9 (Ce4) eV, ascribed to the Ce $3d_{5/2}$, while the other peaks at 898.8 eV (Ce5), 901.9 eV (Ce6), 905.7 eV (Ce7), and 908.4 eV (Ce8) were attributed to Ce $3d_{3/2}$. The higher binding energy satellite peak centered at 917.4 eV (Ce9) is characteristic of Ce^{4+} in the CeO_2. This suggests that cerium exists in the Ce^{4+} oxidation state. On the other hand, the peaks at 884.9 and 901.9 eV are the characteristic peaks of Ce^{3+}. This clearly suggests that both Ce^{4+} and Ce^{3+} ions co-exist in the CeO_2 layers [38–42]. Table 2 lists the atomic percentages of the elements. From the table, the elemental percentage of C 1s, O 1s and Ce 3d in the CeO_2-400 nanostructure was 24.25, 59.58 and 16.17% respectively. Therefore, the higher percentage of C 1s indicates the formation of CeO_2 from the biomass substances.

To evaluate the catalytic performance of the green synthesized CeO_2 nanostructures, the degradation of MB was carried out by $NaBH_4$ in the presence of CeO_2 nanostructures. The characteristic absorption of MB at $\lambda_{max} = 664$ nm was used to monitor the reaction. The effect of annealed temperature of
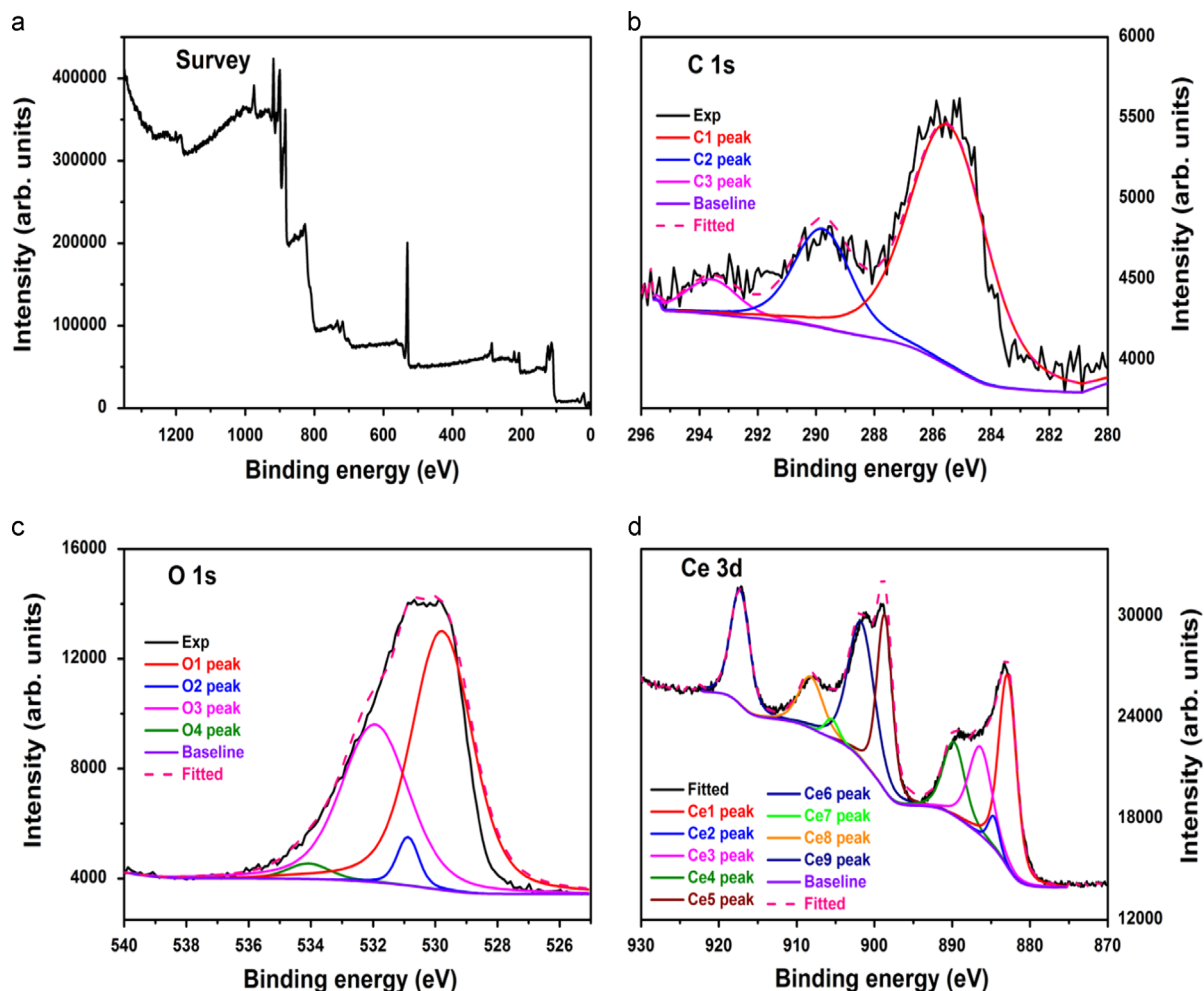
Fig. 5. XPS analysis of the green synthesized CeO$_2$-400 nanostructure: (a) survey scan, and high resolution scans of (b) C 1s, (c) O 1s, and (d) Ce 3d.

Table 2
Atomic weight percentage of C, O and Ce in the CeO$_2$ nanostructure.

Sample	Elemental percentage (at%)		
	C	O	Ce
CeO$_2$-400	24.25	59.58	16.17

CeO$_2$ nanostructures on the catalytic degradation of MB by NaBH$_4$ was examined keeping the other parameters constant. In the absence of CeO$_2$ nanostructure, the mixture of MB and NaBH$_4$ has not shown appreciable degradation (not shown here). Time-dependent variation of absorption spectra of MB by NaBH$_4$ up to 50 min in the presence of CeO$_2$-200, 400 and 600 nanostructures as active catalysts are shown in Fig. 6(a)–(c), respectively. A comparison of the absorption spectra of the catalytically degraded MB after 50 min by NaBH$_4$ in the presence of CeO$_2$ nanostructures is shown in Fig. 6(d). As shown in the figure, after 50 min, the dye concentration of 61.1% (CeO$_2$-200), 52.5% (CeO$_2$-400) and 24.8% (CeO$_2$-600) were degraded from its initial concentration of MB. At higher annealing temperature (600 °C), the CeO$_2$ nanostructure

performed superior catalytic activity against other samples, which are annealed at lower temperatures. C_o and C are the initial and final dye concentrations. The rate of degradation (d%) is given by [39]

$$d\% = \left(1 - \frac{C}{C_o}\right) \times 100\% \qquad (2)$$

where d is the relative percentage degradation of MB (%), C_o and C are the concentration of MB at the initial and time t, respectively. According to the Langmuir–Hinshelwood model, the pseudo-first order kinetic equation for a low dye concentration is given by [43]

$$\ln\left(\frac{C}{C_o}\right) = -kt \qquad (3)$$

where k is the apparent first-order rate constant (min^{-1}). Fig. 6(e) shows a kinetic plot of the pseudo-first-order, $\ln\left(\frac{C}{C_o}\right)$ with respect to time for all annealed samples. All the plots given a linear fit and the slope of the line represents the rate constant (k) for the degradation of the MB dye. The variation of k as a function of annealing temperature of the CeO$_2$ nanostructures is shown in Fig. 6(f). From the figure, it is observed that the rate constants are monotonically increased in
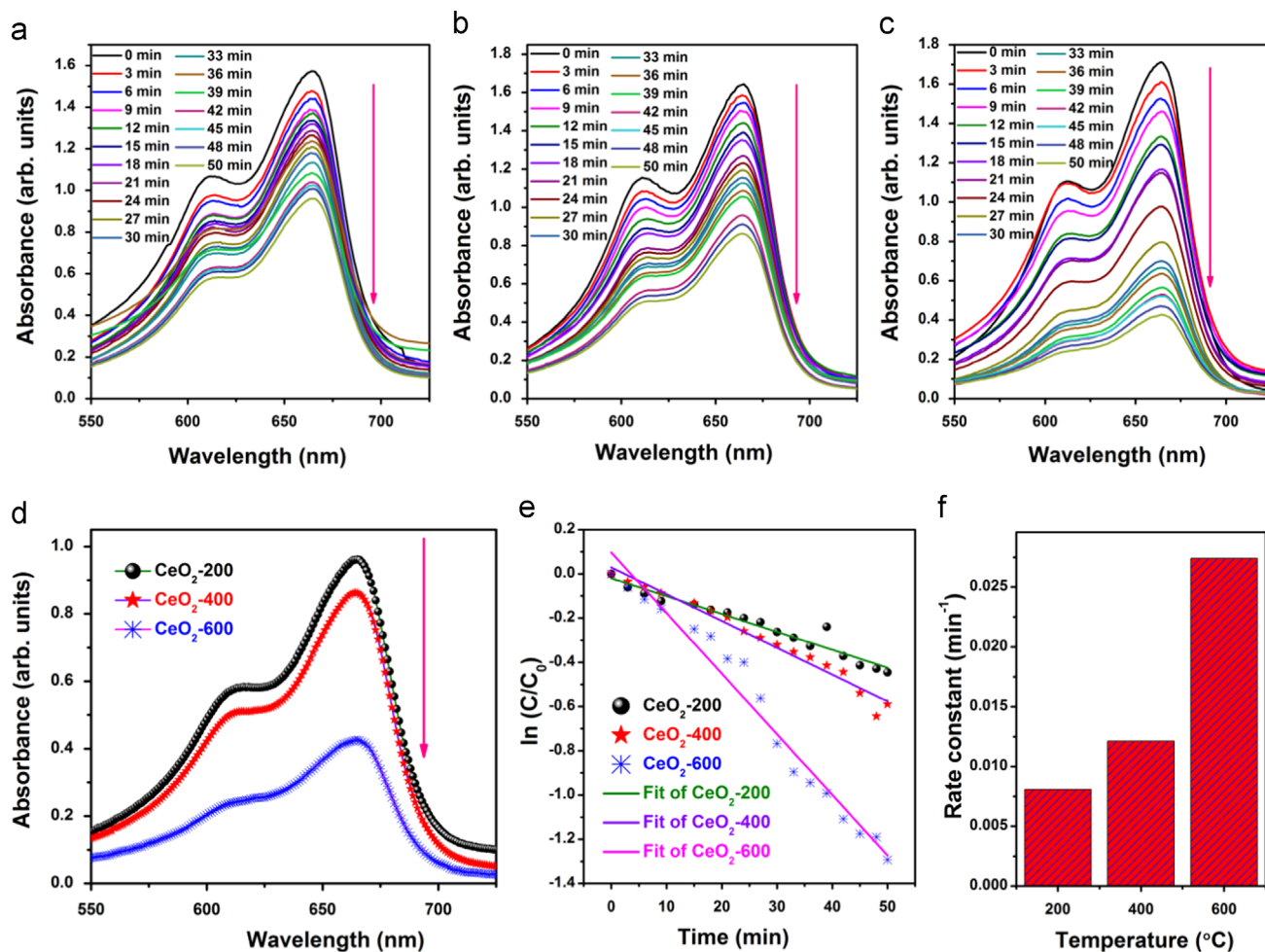
Fig. 6. Time-dependent UV−visible absorption spectra of MB by NaBH$_4$ in the presence of CeO$_2$-200 (a), CeO$_2$-400 (b) and CeO$_2$-600 (c), (d) Comparison of catalytic activity of the annealed samples at 50 min, (e) Plot of $\ln\left(\frac{C}{C_o}\right)$ as a function of time, and (f) Catalytic rate constant of annealed samples.

the following order: CeO$_2$-200 < CeO$_2$-400 < CeO$_2$-600. The CeO$_2$-600 nanostructure performed highest catalytic activity to degradation of MB by NaBH$_4$ with respect to other samples (CeO$_2$-200/400). The efficiency of the catalytic activity of the materials depends on several factors such as, (i) Due to the increase of crystallinity and surface area of the nanomaterials will significantly improve the efficiency of the catalyst, (ii) a decrease in particle size (within the critical size) will also increase the catalytic activity [44–46]. In the present case, the particle/grain size variation of the annealed nanostructures has not in the detectable range (see Fig. 4). Therefore, it is discarded in the present case. However, the improved catalytic activity of the nanostructures is due to the following reasons: (i) the crystallinity of the nanostructures gradually improved against annealing temperatures (Fig. 3(b)) that would turn in reduced the crystalline defects and decreases the density of residual elements from the leaf extracts, (ii) a large surface area of the CeO$_2$-600 nanostructure provides more number of electrons (e$^-$) to improve the e$^-$ transfer reaction from the donor (BH$_4^-$) to acceptor (MB) for the reduction of dye.

4. Conclusion

In summary, the CeO$_2$ nanostructures were synthesized by an eco-friendly green synthesis method using an aqueous bark extract of *P. quassioides*. The formation of the CeO$_2$ nanostructure was monitored using a UV−visible spectrophotometer. The effect of post-annealing temperature on the size−strain values of CeO$_2$ nanostructures were investigated by using X-ray peak broadening method. The obtained crystallite size values from Scherrer method is well consistent with the values calculated in the size−strain plots. The co-existence of Ce^{3+} and Ce^{4+} in the CeO$_2$ nanostructure was confirmed by XPS analysis. A wide-distribution of nanostructures with various polymorphs such as spherical, trigonal, tetragonal, octahedrons, etc was identified by HR-TEM. And the morphology of the nanostructure has not changed appreciably with an increase of annealing temperature. The post-annealing temperature dependent catalytic activity of the cerium oxide nanostructures were carried out for the degradation of MB by NaBH$_4$. The CeO$_2$-600 nanostructure (annealed at 600 °C) showed

significant catalytic activity for the degradation MB by NaBH$_4$. The better catalytic performance of the CeO$_2$-600 is due to the higher crystallinity and large surface area as compared to other samples.

Acknowledgments

References

[1] Z. Hu, S. Haneklaus, G. Sparovek, E. Schnug, Rare earth elements in soils, Commun. Soil Sci. Plant Anal. 37 (2006) 1381–1420.

[2] J.J. Miao, H. Wang, Y.R. Li, J.M. Zhu, J.J. Zhu, Ultrasonic-induced synthesis of CeO$_2$ nanotubes, J. Cryst. Growth 281 (2005) 525–529.

[3] X. Jiao, H. Song, H. Zhao, W. Bai, L. Zhang, Y. Lv, Well-redispersed ceria nanoparticles: promising peroxidase mimetics for H$_2$O$_2$ and glucose detection, Anal. Methods 4 (2012) 3261–3267.

[4] Q. Fu, H. Saltsburg, M. Flytzani-Stephanopoulos, Active non-metallic Au and Pt species on ceria-based water–gas shift catalysts, Science 301 (2003) 935–938.

[5] P. Jasinski, T. Suzuki, H.U. Anderson, Nanocrystalline undoped ceria oxygen sensor, Sens. Actuators B: Chem. 95 (2003) 73–77.

[6] D.G. Shchukin, R.A. Caruso, Template synthesis and photocatalytic properties of porous metal oxide spheres formed by nanoparticle in filtration, Chem. Mater. 16 (2004) 2287–2292.

[7] A. Martinez-Arias, A.B. Hungria, M. Fernandez-Garcia, A. Iglesias-Juez, J.C. Conesa, G.C. Mather, G. Munuera, Cerium–terbium mixed oxides as potential materials for anodes in solid oxide fuel cells, J. Power Sources 151 (2005) 43–51.

[8] S. Yabe, T. Sato, Cerium oxide for sunscreen cosmetics, J. Solid State Chem. 171 (2003) 7–11.

[9] R. Li, S. Yabe, M. Yamashita, S. Momose, S. Yoshida, S. Yin, T. Sato, Synthesis and UV-shielding properties of ZnO and CaO-doped CeO$_2$ via soft solution chemical process, Solid State Ion. 151 (2002) 235–241.

[10] H. Yahiro, Y. Baba, K. Eguchi, A. Hiromichi, High temperature fuel cell with ceria-yttria solid electrolyte, J. Electrochem. Soc. 135 (1998) 2077–2080.

[11] P. Zhang, Y. Ma, Z. Zhang, X. He, J. Zhang, Z. Guo, R. Tai, Y. Zhao, Z. Chai, Biotransformation of ceria nanoparticles in cucumber plants, ACS Nano 11 (2012) 9943–9950.

[12] F. Goubin, X. Rocquefelte, M.H. Whangbo, Y. Montardi, R. Brec, S. Jobic, Experimental and theoretical characterization of the optical properties of CeO$_2$, SrCeO$_3$, and Sr$_2$CeO$_4$ containing Ce^{4+} (f$_0$) ions, Chem. Mater. 16 (2004) 662–669.

[13] S. Patil, A. Sandberg, E. Heckert, W. Self, S. Seal, Protein adsorption and cellular uptake of cerium oxide nanoparticles as a function of zeta potential, Biomaterials 28 (2007) 4600–4607.

[14] F. Zhang, S.W. Chan, J.E. Spanier, E. Apak, Q. Jin, R.D. Robinson, I. P. Herman, Cerium oxide nanoparticles: size-selective formation and structure analysis, Appl. Phys. Lett. 80 (2002) 127–129.

[15] X.H. Liao, J.M. Zhu, J.J. Zhu, J.Z. Xu, H.Y. Chen, Preparation of monodispersed nanocrystalline CeO$_2$ powders by microwave irradiation, Chem. Commun. 10 (2001) 937–938.

[16] H. Wang, J.J. Zhu, J.M. Zhu, X.H. Liao, S. Xu, T. Ding, H.Y. Chen, Preparation of nanocrystalline ceria particles by sonochemical and microwave assisted heating methods, Phys. Chem. Chem. Phys. 4 (2002) 3794–3799.

[17] F. Czerwinski, J.A. Szpunar, The nanocrystalline ceria sol-gel coatings for high temperature applications, J. Sol–Gel Sci. Technol. 9 (1997) 103–114.

[18] C. Sun, H. Li, H. Zhang, Z. Wang, L. Chen, Controlled synthesis of CeO$_2$ nanorods by a solvothermal method, Nanotechnology 16 (2005) 1454–1463.

[19] J.-d Hu, Y.-x Li, X.-z Zhou, M.-x Cai, Preparation and characterization of ceria nanoparticles using crystalline hydrate cerium propionate as precursor, Mater. Lett. 61 (2007) 4989–4992.

[20] T.P. Yadav, O.N. Srivastava, Synthesis of nanocrystalline cerium oxide by high energy ball milling, Ceram. Int. 38 (2012) 5783–5789.

[21] Y. Wang, T. Mori, J.-G. Li, T. Ikegami, Low temperature synthesis of praseodymium-doped ceria nanopowders, J. Am. Ceram. Soc. 85 (2002) 3105–3107.

[22] S.-Y. Yao, Z.-H. Xie, Deagglomeration treatment in the synthesis of doped-ceria nanoparticles vis coprecipitation route, J. Mater. Process. Technol. 186 (2007) 54–59.

[23] S. Maensiri, C. Masingboon, P. Laokul, W. Jareonboon, V. Promarak, P. L. Anderson, S. Seraphin, Egg white synthesis and photoluminescence of plate like clusters of CeO$_2$ nanoparticles, Cryst. Growth Des. 7 (2007) 950–955.

[24] A. Arumugam, C. Karthikeyan, A.S.H. Hameed, K. Gopinath, S. Gowri, V. Karthika, Synthesis of cerium oxide nanoparticles using Gloriosa superba L. leaf extract and their structural, optical and antibacterial properties, Mat. Sci. Eng. C 49 (2015) 408–415.

[25] G. Sai Priya, A. Kanneganti, K. Anil Kumar, K. Venkateswara Rao, Satish Bykkam, Biosynthesis of cerium oxide nanoparticles using Aloe barbadensis miller gel, Int. J. Sci. Res. Publ. 4 (2014) 1–4.

[26] Chinese Material Medical Committee, Zhonghua Bencao, 2nd ed., Shanghai Science and Technology Press Shanghai, China, 1998.

[27] Pharmacopoeia Committee, Pharmacopoeia of the People's Republic of China, vol. 1, China Medical Science and Technology Press, Beijing, China, 2010.

[28] S. Kundu, N. Sutradhar, R. Thangamuthu, B. Subramanian, A.B. Panda, M. Jayachandran, Fabrication of catalytically active nanocrystalline samarium (Sm) doped cerium oxide (CeO$_2$) thin films using electron beam evaporation, J. Nanoparticle Res. 14 (2012) 1–16.

[29] N. Uekawa, Y.M. Ueta, J. Wu, K. Kakegawa, Characterization of CeO$_2$ fine particles prepared by the homogeneous precipitation method with a mixed solution of ethylene glycol and polyethylene glycol, J. Mater. Res. 19 (2004) 1087–1092.

[30] S.B. Khan, M. Faisal, M.M. Rahman, A. Jamal, Exploration of CeO$_2$ nanoparticles as a chemi-sensor and photo-catalyst for environmental applications, Sci. Total Environ. 409 (2011) 2987–2992.

[31] B. Yan, H.X. Zhu, Controlled synthesis of CeO$_2$ nanoparticles using novel amphiphilic cerium complex precursors, J. Nanopart. Res. 10 (2008) 1279–1285.

[32] R.C. Deus, M. Cilense, C.R. Foschini, M.A. Ramirez, E. Longo, A. Z. Simões, Influence of mineralizer agents on the growth of crystalline CeO$_2$ nanospheres by the microwave- hydro thermal method, J. Alloy. Compd. 550 (2013) 245–251.

[33] C. Rajesh, G. Kruthika, G. Govindaraj, L. Vijayan, Electrical relaxation studies of olivine type nanocrystalline LiMPO$_4$ (M=Ni, Mn, and Co) materials, J. Phys. Chem. Solids 86 (2015) 27–35.

[34] G.R. Dillip, B. Ramesh, C. Madhukar Reddy, K. Mallikarjuna, O. Ravi, S.J. Dhoble, S.W. Joo, B. Deva Prasad Raju, X-ray analysis and optical studies of Dy^{3+} doped NaSrB$_5$O$_9$ microstructures for white light generation, J. Alloy. Compd. 615 (2014) 719–727.

[35] B. Ramesh, G. Devarajulu, B. Deva Prasad Raju, G. Bhaskar Kumar, G. R. Dillip, A.N. Banerjee, S.W. Joo, Determination of strain, site occupancy, photoluminescent, and thermoluminescent-trapping parameters of Sm^{3+}-doped NaSrB$_5$O$_9$ microstructures, Ceram. Int. 42 (2016) 1234–1245.

[36] S. Hazarika, D. Mohanta, Extraction and characterization of mixed phase KNO$_2$–KNO$_3$ nanocrystals derived from flat-leaf green spinach, Phys. Scr. 87 (2013) 015603.

[37] Z.L. Wang, X. Feng, Polyhedral Shapes of CeO$_2$ Nanoparticles, J. Phys. Chem. B 107 (2003) 13563–13566.

[38] L. Martinez, E. Roman, J.L. de Segovia, S. Poupard, J. Creus, F. Pedraza, Surface study of cerium oxide based coatings obtained by cathodic electrodeposition on zinc, Appl. Surf. Sci. 257 (2011) 6202–6207.

[39] G.R. Dillip, A.N. Banerjee, V.C. Anitha, S.W. Joo, B.K. Min, S. Y. Sawant, M.H. Cho, Anchoring mechanism of ZnO nanoparticles on graphitic carbon nanofiber surfaces through a modified co-precipitation method to improve interfacial contact and photocatalytic performance, ChemPhysChem 16 (2015) 3214–3232.

[40] X. Chen, G. Li, Y. Su, X. Qiu, L. Li, Z. Zou, Synthesis and room temperature ferromagnetism of CeO$_2$ nanocrystals with nonmagnetic Ca^{2+} doping, Nanotechnology 20 (2009) 115606–115613.

[41] E. Beche, P. Charvin, D. Perarnau, S. Abanades, G. Flamant, Ce 3d XPS investigation of cerium oxides and mixed cerium oxide (Ce$_x$Ti$_y$O$_z$), Surf. Interface Anal. 40 (2008) 264–267.

[42] B.M. Reddy, A. Khan, Y. Yamada, T. Kobayashi, S. Loridant, J.C. Volta, Structural Characterization of CeO$_2$–TiO$_2$ and V$_2$O$_5$/CeO$_2$–TiO$_2$ catalysts by Raman and XPS techniques, J. Phys. Chem. B 107 (2003) 5162–5167.

[43] T.D. Dang, A.N. Banerjee, S.W. Joo, B.K. Min, Synthesis of amorphous and crystalline hollow manganese oxide nanotubes with highly porous walls using carbon nanotube templates and enhanced catalytic activity, Ind. Eng. Chem. Res. 53 (2014) 9743–9753.

[44] B. Paul, B. Bhuyan, D.D. Purkayastha, M. Dey, S.S. Dhar, Green synthesis of gold nanoparticles using *Pogestemon benghalensis* (B) *O. Ktz.* leaf extract and studies of their photocatalytic activity in degradation of methylene blue, Mater. Lett. 148 (2015) 37–40.

[45] J. Lin, X. Liu, S. Zhu, Y. Liu, X. Chen, Anatase TiO$_2$ nanotube powder film with high crystallinity for enhanced photocatalytic performance, Nanoscale Res. Lett. 10 (2015) 110.

[46] S. Bhakya, S. Muthukrishnan, M. Sukumaran, M. Muthukumar, T. S. Kumar, M.V. Rao, Catalytic degradation of organic dyes using synthesized silver nanoparticles: a green approach, J. Bioremediat. Biodegrad. 6 (2015) 5.